Comparing ice cloud microphysical properties using CloudNET and Atmospheric Radiation Measurement Program data

G.-J. van Zadelhoff, D. P. Donovan, H. Klein Baltink, and R. Boers

Royal Netherlands Meteorological Institute, De Bilt, Netherlands

[1]   A comparison of the microphysical properties of ice clouds, using lidar and radar data, is made for three sites: Cabauw (Netherlands), Atmospheric Radiation Measurement Program Southern Great Plains (ARM-SGP) site (United States), and Chilbolton (United Kingdom). The effective particle size (R_{eff}), extinction, and ice water content (IWC) are derived and correlated to each other, temperature, radar reflectivity, and depth into the cloud from cloud top (ΔZ_t). There is no indication for large seasonal differences of the ice microphysical properties; however, the R_{eff} differences observed at the ARM-SGP site are of the same magnitude as the error. The Chilbolton and Cabauw sites exhibit similar behavior in all cases while the ARM site shows large differences for some relationships, e.g., $R_{\mathrm{eff}}(T, \mathrm{IWC})$. Within the sensitivity studies performed, it is not possible to construct a single $R_{\mathrm{eff}}(T, \mathrm{IWC})$ parameterization valid at all three sites, and therefore it is not applicable in global models. It is possible to construct a single parameterization of ice water content related to temperature or to radar reflectivity. In all cases, an ice habit and particle size distribution assumption has to be made, resulting in different fits for different habits. When R_{eff} is correlated to ΔZ_t for different classes of total cloud thicknesses (H), one can define a single parameterization, using parabolic descriptions, valid at the three sites and possibly on a global scale.   *INDEX TERMS:* 0320 Atmospheric Composition and Structure: Cloud physics and chemistry; 0360 Atmospheric Composition and Structure: Transmission and scattering of radiation; 3359 Meteorology and Atmospheric Dynamics: Radiative processes; *KEYWORDS:* lidar radar, ice clouds, effective ice crystal sizes

1.   Introduction

[2]   The importance of ice clouds for the Earth's radiation budget is well recognized [*Arking*, 1991]. Cirrus clouds, consisting predominantly of ice crystals, cover more than 20% of the globe [*Wylie and Menzel*, 1999] and, depending on their optical thickness, altitude and microphysical properties, can cause either warming (greenhouse effect) or cooling (albedo effect) at the Earth's surface.

[3]   Because of uncertainties concerning the properties of ice clouds and the complex interactions between microphysics and radiation in these clouds, as well as the dynamics of the environment [*Quante and Starr*, 2002], ice clouds are not well treated in climate and forecasting models. Advances in the treatment of ice clouds in general circulation models (GCMs) and cloud-resolving models will require not only better resolution but also a better description of the microphysical and radiative properties of ice clouds. For this, a better understanding of the properties of ice cloud particle distributions is needed.

[4]   Cloud radiative properties, such as single-scattering albedo and asymmetry factor, needed to model the impact of ice clouds on atmospheric flux profiles are often linked to the effective size of the ice crystal particles. One such measure of effective size is the effective radius (R_{eff}). For a distribution of nonspherical ice particles the effective radius is defined as

$$R_{\mathrm{eff}} = \frac{3}{4\rho_{s,i}} \frac{\langle M(D)\rangle}{\langle A_c(D)\rangle} = \frac{3}{2} \frac{\mathrm{IWC}}{\rho_{s,i}\alpha}, \qquad (1)$$

where the braces denote averaging over the particle size distribution, D denotes the maximum dimension of the particle, M denotes the particle mass, A_c denotes the cross-sectional area, $\rho_{s,i}$ denotes the density of solid ice and α denotes the extinction where $\alpha = 2N_0\langle A_c(D)\rangle$ and N_0 is the total number of particles.

[5]   Parameterizations of R_{eff} versus temperature for different ice habits have been included in a few GCMs. In particular, *Kristjánsson et al.* [2000] found that including a temperature-dependent effective particle size parameterization resulted in significant radiative warming in the upper tropical troposphere and at high latitudes compared to the case where a globally uniform single-size ice particle size distribution was used.

Table 1. Instruments Used in the Comparison of the Three Sites

| | | Lidar | | Pressure and | |
	Radar Frequency	Name	λ, nm	Temperature	Period
ARM	35 GHz	MPL	532	sondes	Nov. and Dec. 1996, July 1997, and Jan. and July 2000
Cabauw	35 GHz	CT-75K	905	ECMWF	Oct. 2001 to June 2003
Chilbolton	94 GHz	CT-75K	905	ECMWF	Oct. 2001 to March 2002

[6] Most ice cloud effective radius parameterizations have been based on in situ data acquired during dedicated campaigns within limited time periods [e.g., *Heymsfield and McFarquhar*, 2002]. Recently, temperature-dependent parameterizations have been developed using combined lidar and radar data acquired at the Atmospheric Radiation Measurement (ARM) Program's Southern Great Plains (SGP) site [*Donovan and van Lammeren*, 2002; *Donovan*, 2003; *Wang and Sassen*, 2002]. The use of remotely sensed particle size profiles enables the use of long continuous periods of data retrievals, resulting in more than a couple hundred thousand observed ice cloud points over time periods spanning months.

[7] In this work, a comparison is made between ice cloud effective particle sizes derived from lidar and radar data at three different sites. In particular, the same ARM-SGP data that were used in the study of *Donovan* [2003] are compared to data acquired at Chilbolton in the United Kingdom and at Cabauw in the Netherlands as part of the EU-funded CloudNet program. By comparing the three sites, we intend to check if there is a consistent single parameterization that explains the observed ice cloud effective particles sizes at all three sites.

[8] The outline of the paper is as follows. In section 2 the procedure used to calculate the microphysical properties is discussed. Section 3 gives an overview of the different observation sites from which data are used. In section 4 the results for the Cabauw site are presented using all the observed ice clouds. From this data set a subset is taken and compared to the ARM site results in section 5. The effective particle size correlated to cloud depth is presented in section 6. Finally, in section 7, the main conclusions are given.

2. Lidar/Radar Inversion Procedure

[9] The cloud microphysical properties used in this work have been derived using both lidar and radar signals. The procedure used to calculate the properties has been extensively described by *Donovan and van Lammeren* [2001] and *Donovan et al.* [2001]. In this section, a short summary of the procedure is given.

[10] The lidar/radar algorithm used in this work is based on an inversion procedure where the lidar extinction coefficient (α) is calculated using a Klett-type solution procedure [*Klett*, 1981] with an appropriate boundary value. As the extinction can be directly related to the single-scattering power at the lidar wavelength, it is important to correctly calculate the fraction of the observed signal due to multiple scattering. The effect of multiple scattering on the lidar return is approximately accounted for by the analytical model of *Eloranta* [1998]. This approach gives good results, compared to full Monte Carlo calculations, for small lidar opening angles.

[11] In the retrieval the vertical profiles of the lidar-derived extinction and radar reflectivity (Z_e) are combined to derive particle sizes. The effective radius R_{eff} is not directly estimated; instead first a lidar/radar effective radius (R'_{eff}) is estimated. This R'_{eff} is then used to estimate the true R_{eff}.

[12] The lidar/radar effective radius is defined as

$$\left(R'_{\mathrm{eff}}\right)^4 = \frac{9}{16\pi\rho_{s,i}^2} \frac{\langle M^2(D)\rangle}{\langle A_c(D)\rangle} = R_{\mathrm{eff}} \frac{3}{4\pi\rho_{s,i}} \frac{\langle M^2(D)\rangle}{\langle M(D)\rangle}, \qquad (2)$$

where equation (1) is used to link the two different effective radii definitions. The fraction $\langle M^2(D)\rangle/\langle M(D)\rangle$ depends on the precise particle size distribution and ice crystal habit.

[13] As Z_e is determined by the squared mass distribution and the extinction by the total cross-sectional area of the particles, R'_{eff} is an invariant function of the ratio between the optical extinction and the radar reflectivity:

$$\left(R'_{\mathrm{eff}}\right)^4 \propto \frac{Z_e}{\alpha}, \qquad (3)$$

where α is the extinction at the lidar wavelength and Z_e is the radar reflectivity. This is valid at least in the regime where the particle sizes are in the Rayleigh regime at the radar frequency and are optical scatterers at the lidar wavelength.

[14] To conclude, R'_{eff} is defined by the observations only. No assumption needs to be made concerning the particle size distribution and ice crystal habit as these are not derived quantities. However, the conversion to the true effective radii (R_{eff}) does depend on assumptions made about the true ice crystal habit and the size distribution characteristics; in particular, the degree of multimodality is important [*Donovan*, 2003].

3. Observations

[15] In this comparison we make use of data from three facilities. The U.S. Southern Great Plains site established by the Atmospheric Radiation Measurement (ARM) Program, from here on referred to as the ARM site, is the first site. The other two sites, Cabauw (Netherlands) and Chilbolton (Great Britain), are participants in the CloudNET research project. The different instruments used at each of the sites, the periods examined and the sources of temperature and pressure data are listed in Table 1.

[16] The observations at Cabauw form a continuous data set from October 2001 up to June 2003. The Chilbolton data set is shorter because of problems with their radar, which was taken off-line in 2002 but has been fully operational since April 2003. The radar data in the period from October 2001 to March 2002 are assumed to be correct for reflectivities larger than −20 dBZ only. The influence of this lower limit on the results is presented in section 5.2.2 and

Appendix A. The data set taken from the ARM site spans several months in the period between 1996 and 2000. The correct calibration of the radar is of crucial importance for the derivation of the microphysical properties of clouds. The radars at Cabauw and Chilbolton have recently (March 2004) been intercalibrated with each other using the French Rasta mobile 94 GHz radar. They were found to be within 3 dBZ of each other (D. Bouniol, private communications, 2004), similar to what was found in 2001 during the BBC campaign. The ARM radar has been checked 3 times per month and calibrated to both the NOAA Ka band and a smaller radar antenna and should be within 2 dBZ (K. Widener, private communications, 2004). The main difference between the sites is the sensitivity of the different lidars. At both the CloudNET sites there is a CT-75K ceilometer, while at the ARM site the Micropulse Lidar was used. The latter instrument is superior in power-aperture product and has a smaller field of view, making the influence on the received signal due to multiple scattering less of an issue. For details on the different instruments and sites we refer the reader to the appropriate web sites: http://www.arm.gov/sites/sgp.stm and http://www.met.rdg.ac.uk/radar/cloudnet for the ARM site and CloudNET sites, respectively.

4. General Cloud Comparison

[17] Cloud microphysical parameters can only be calculated for a cloud observed by both the radar and the lidar. This immediately limits the sample to a subset of clouds. In general, the radar is, in contrast to the lidar, not limited by extinction of its beam. However, for very small particles, the radar backscatter becomes too small to be detectable. This can lead to undetected clouds consisting of very small particles ($R_{eff} < 10$ μm) or a wrong determination of the cloud boundaries. (The particle size limitation is demonstrated in Figure A1 (Appendix A), where the effects of a lower limit to the radar reflectivity are assessed.) The lidar, on the other hand, is limited by extinction within the clouds. This means that in the case of optically thick clouds ($\tau > 4$), the lidar beam is often not able to penetrate the entire cloud but only the lower part.

[18] In Figure 1, the retrieved lidar/radar effective particle sizes for the entire period of Cabauw observations are shown. The contour lines and greyscale show the cumulative probability of occurrence of all observations. These are defined by first counting the number of occurrences within each grid box, after which each is tested for the number of grid boxes with an equal or higher number of occurrences; for example, the 60% contour line of occurrence surrounds the grid boxes for which 60% of all grid boxes have an equal or higher number of occurrences. The mean is calculated for all observed values within a temperature bin. The temperature-versus-R_{eff}' relation observed at Cabauw shows significantly different behavior when compared to the ARM site for which the mean is overlaid [*Donovan and van Lammeren*, 2002, Figure 2]. The third site, Chilbolton, was not included in this comparison. Because of problems with the Galileo radar at Chilbolton (before March 2003) only signals higher than −20 dBZ are available. This excludes a large portion of the observed data. It also raises the question as to whether you can directly
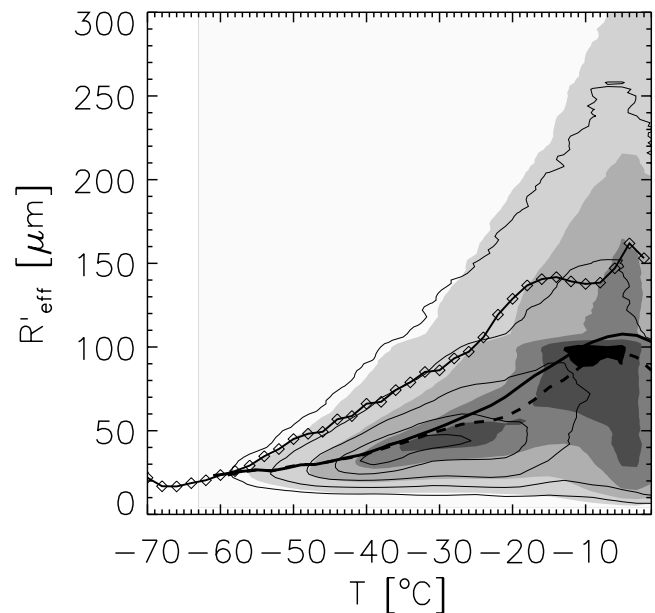

Figure 1. Cumulative probability of occurrence of R_{eff}' as a function of temperature for all observed clouds at Cabauw. The greyscale, from dark to light, shows the 10, 30, 60, 90 and 99% probability of occurrence (see section 4). The thick solid line shows the mean particle size at each temperature. The solid line with diamonds is the mean particle size as deduced from the ARM data. The contour lines depict the probability of occurrence in the case of clouds with optical thickness less than 4, with the dashed line showing the corresponding mean (section 5).

compare this to the other two sites. In Appendix A, a sensitivity study is performed to check for the dependence of the microphysical parameters on the radar signal. As the radar reflectivity (Z_e) is strongly influenced by the particle size, a lower limit on the radar reflectivity directly influences the range of observed particle sizes. The mean $R_{eff}'(T)$ relationships observed at the ARM and Cabauw sites are shown to be well converged for the lower limit on their radar signals, this in contrast to the Chilbolton results.

[19] A direct comparison as presented in Figure 1 can be misleading. The use of the different instruments at the different sites (Table 1) can result in different cloud samples; for example, the Micropulse Lidar (MPL) can probe optically thicker regimes compared to the CT-75K, and the CT-75K also has more problems in detecting clouds during daytime compared to nighttime (Appendix B, Figure B1) because of an increase in background noise.

[20] In order to make it possible to consistently compare the data sets, a subset is defined for all three sites. The subset is limited to those clouds that were fully visible in both the lidar and the radar simultaneously; that is, the tops of the cloud in both the radar and the lidar should be similar. The clouds in the subset are referred to in this work as optically thin ice clouds, with no other meaning than that the entire cloud can be seen and not that the total optical depth is smaller than 1. In reality, the clouds fulfilling the criteria can reach optical depths up to $\tau \sim 4$. In the case of Cabauw, 21%(=246,000 points) of all available points observed by both lidar and radar are within clouds that

have the same lidar and radar vertical extent. From the ARM site a similar number of points are available (295,000). The influence on the distribution by taking this subset is a shift in the peak of the cumulative probability of occurrence of R'_{eff} to lower temperatures, with the peak shifting from $-10°$ to $-35°C$ (Figure 1, greyscale compared to contour lines). The mean R'_{eff}, however, shifts only by ~ 10 μm at the higher temperatures, which is less than the difference between the Cabauw and ARM sites and is within the error in the mean of $10-20\%$.

5. Optically Thin ($\tau_{vis} \leq 4$) Ice Clouds

[21] As discussed in section 4, the analysis of the data is limited to a subset in order to consistently compare the data obtained at the ARM site and the two CloudNET sites. Accordingly, only clouds that were fully resolved in both the lidar and radar were chosen for comparison. In this case, the sets of data are comparable, and the difference of cloud microphysics can be compared directly in a similar way. One has to keep in mind that this reduces the data sets to optically thin ($\tau_{vis} \leq 4$) clouds and therefore is not, by definition, applicable to the entire set of ice clouds.

5.1. Cloud Statistics

[22] To illustrate the differences in the observed clouds at the three different sites, a comparison is made between the height and geometrical thickness distributions of the observed clouds at each of the sites.

[23] The height distribution is calculated for all detected cloudy pixels, after which the distribution is normalized. The resulting histogram (Figure 2) shows a large difference between the ARM site and the two coastal European sites. The ARM site has higher clouds (reaching up to 16 km) and a wider distribution compared to the other two (up to 12 km). These distributions are compared to observations taken with HIRS [*Wylie and Menzel*, 1999]. This data set provides monthly statistics from 11 years of HIRS data (the data are available from D. P. Wylie at ftp://ftp.ssec.wisc.edu/). To make sure that a consistent comparison is made, the cloud profiles of only the IR transmissive clouds are taken into account (Figure 2). The HIRS results were combined using the observed lidar/radar monthly fractions to include any seasonal variability seen in the directly observed distributions.

[24] The HIRS and lidar/radar data show similar results. Even though clouds are seen up to 16 km for all three sites with HIRS, the clouds higher than 11 km lie in the tail of the distribution for the two European sites. The CT-75K as well as the radar at the Cabauw site are optimized for detecting clouds below 12 km, thereby making sure that the tail of the distribution as observed by HIRS is missing in the lidar radar observations. The Cabauw and Chilbolton data show similar distributions while the distribution observed at the ARM site is shifted upward by $2-3$ km. The difference in width of the distribution might be caused by several things. First, the sets of clouds are not the same. There are more clouds in the HIRS database as lidar extinction poses a more severe constraint than the IR transmissivity in accepting clouds for the comparison. Second, the HIRS database is based on the CO_2 slicing method [*Wylie and Menzel*, 1999], which in turn can result in height errors, which might result
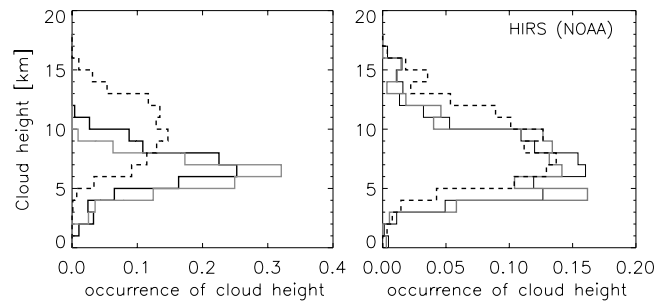

Figure 2. Normalized cloud height occurrence at the three sites considered, Cabauw (solid black lines), Chilbolton (solid grey lines) and ARM (dashed lines). Cloud height occurrence as observed (left) using the lidar/radar method and (right) using HIRS data.

in broader distributions. Third, the ARM lidar is more powerful than the CT-75K, and it could easily be the case that the thicker clouds are rejected by the algorithm for the two sites with the CT-75K lidar.

[25] One of the reasons to choose only ice clouds that are fully penetrated is to get a similar sample of clouds. A benefit of this sample is that it provides the opportunity to define both the cloud top and the cloud bottom. The cloud top is defined as the top of the last pixel that has both a reliable radar signal and a reliable lidar signal. This introduces an uncertainty of one or two range gates as the radar and lidar signals do not always end at exactly the same point, leading to a vertical error estimate of $100-200$ m. Furthermore, there is the possibility that the true upper part of the cloud has such small particles that the radar is not able to detect them and that at the same time the lidar has reached its maximum extinction and therefore shows no signal. These types of cases are missed at both Cabauw and ARM sites. Even though it is difficult to make sure that the boundaries defined are the true exact cloud edges, the definition is the same for all the cases, and the true cloud thickness is most likely close to the one given here. In Figure 3 the histograms of cloud thickness occurrence are shown to see whether the observed width of the distributions is due to thin clouds or thick clouds. From Figure 3 it can be seen that thicker clouds were observed over the ARM site than were observed over Cabauw. However, the most probable cloud thickness occurrence (at around $1-1.5$ km) is not that different at the two sites. The Chilbolton site shows a similar histogram for $Z_e > -20$ dBZ.

5.2. Microphysical Parameters of Ice Clouds

[26] *Donovan and van Lammeren* [2002] and *Donovan* [2003] extensively discussed the particle sizes derived for the ARM site. The data used in this paper are, as mentioned, a subset of the total data in the sense that only fully penetrated clouds are taken into account. The results presented in those papers also generally apply to the subset of data used here, including the relationships between R'_{eff} versus temperature and IWC'. The differences due to the subset for the ARM site are similar to the impact of the subset on the results shown previously in Figure 1 for the Cabauw data.

[27] In this section, most of the particle sizes are given as the lidar/radar effective radius (R'_{eff}) and lidar/radar effec-
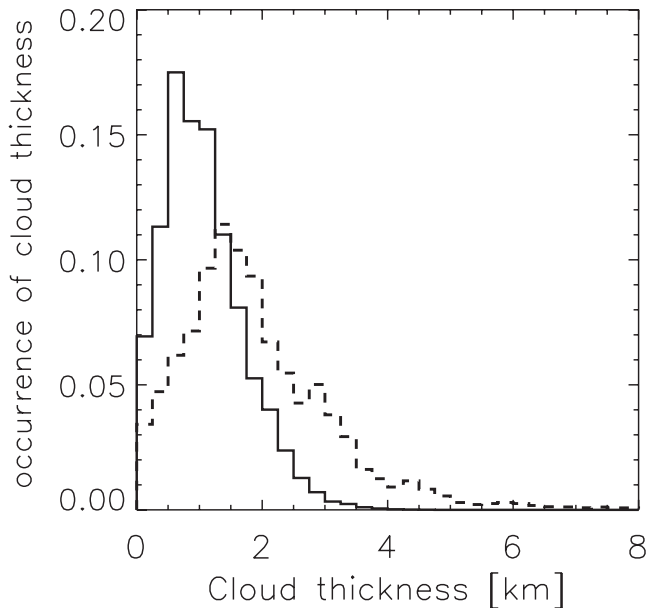
Figure 3. Normalized cloud thickness occurrence at Cabauw (solid line) and the ARM site (dashed line).

tive ice water content (IWC′). For those few cases when R_{eff} or IWC is used, the particles are assumed to have a complex polycrystal habit and consist of a bimodal density distribution adopting the fit results from *Donovan* [2003]. A comparison is made for R_{eff} and IWC for different habits in Appendix C. In the following sections, the Cabauw and ARM sites are compared to each other, except for section 5.2.2, where both these sites are compared to the results obtained from the Chilbolton site.

5.2.1. Particle Sizes

[28] In this section, R'_{eff} is correlated with temperature, measured Doppler velocity, and cloud depth seen from cloud top.

[29] In the literature there has been much emphasis on finding particle size to temperature relationships [e.g., *Boudala et al.*, 2002; *Garrett et al.*, 2003] for use in GCM models [*Kristjánsson et al.*, 2000], or particle sizes in relation to a combination of temperature and IWC (e.g., *McFarquhar et al.* [2003] (see their Table 1 for an overview) and *Donovan* [2003]). It is therefore of interest to see if the different sites can be described by the same parameterization. In Figure 1 it can be seen that the ARM and Cabauw data show significant differences with respect to their respective $R'_{eff}(T)$ relationships. This difference remains for the subsample.

[30] Before looking at the $R'_{eff}(T)$ relationships for the defined subset, the effective particle sizes are first correlated to their measured Doppler velocities (Figure 4).

[31] For a given ambient temperature and pressure, the terminal velocity of an ice crystal is a strong function of the particle's area-to-mass ratio [*Heymsfield and Iaquinta*, 2000; *Heymsfield*, 2003]. Thus a relationship between V_d and R_{eff} (and hence R'_{eff}) is to be expected. However, the exact relationship between R'_{eff} and V_d will depend on the exact form of the size distribution and the relationship between mass, area, and crystal maximum dimension (i.e., the crystal habit). The relationship between V_d and R'_{eff} for
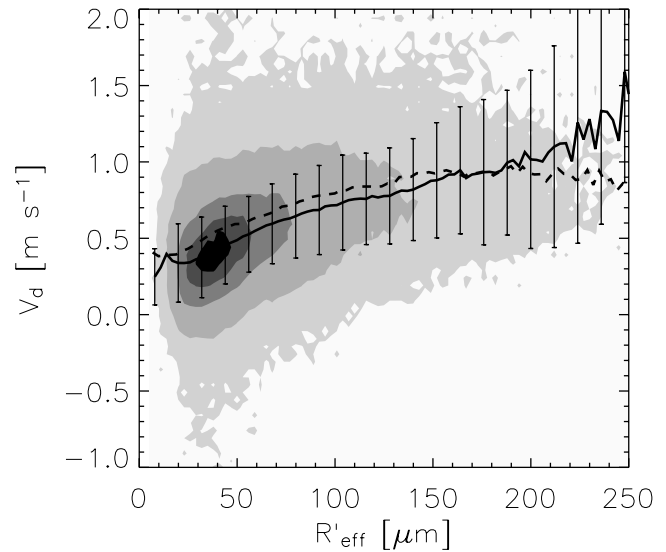

Figure 4. Probability density plot of the occurrence of the Doppler velocity as measured by the radar to the calculated R'_{eff} for optically thin ($\tau_{vis} \leq 4$) clouds at Cabauw. The greyscale, from dark to light, shows the 10, 30, 60, 90 and 99% probability of occurrence. The solid line shows the mean Doppler velocity for each particle size bin, where a bin size of 3 μm was used. The error bars indicate the 1σ level of the distribution. The dashed line shows the mean V_d for each R'_{eff} from the ARM data.

unimodal modified gamma type size distributions is shown in Figure 5 (black lines) for three different crystal habits. The corresponding relationships between V_d and R_{eff} (grey lines) are also plotted to enable an easier comparison with
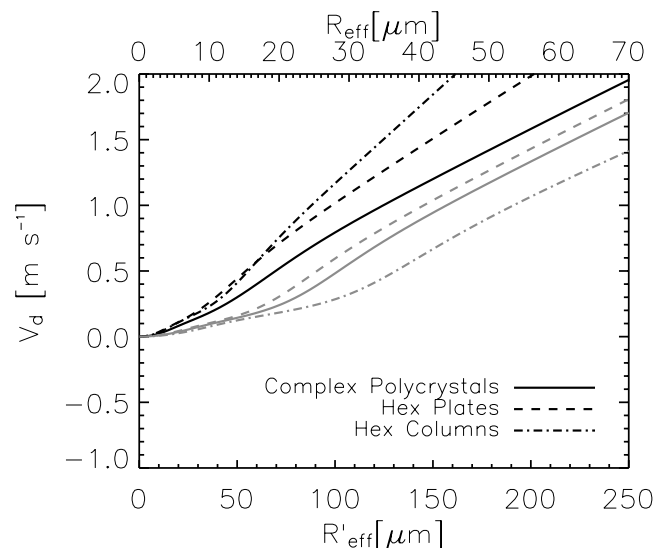

Figure 5. Modeled Doppler velocity to R'_{eff} and R_{eff} relationship for three types of habits: complex polycrystals (solid lines), hex plates (dashed lines) and hex columns (dot-dashed lines). The black lines show the V_d-R'_{eff} relationships, with the scaling on the lower x axis. The grey lines show the V_d-R_{eff} relationships, with the scaling on the upper x axis. Note that the R_{eff} scale is chosen for clarity and cannot be directly related to the R'_{eff} scale.
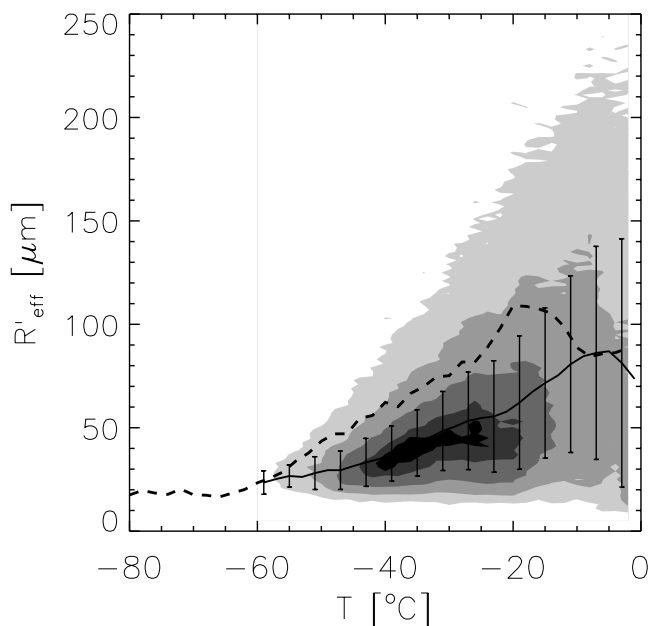
Figure 6. Cumulative probability of occurrence of R'_{eff} as a function of temperature for optically thin ($\tau_{vis} \leq 4$) clouds at Cabauw. The greyscale and annotations follow the same scheme as in Figure 4. The dashed line shows the mean particle size for the ARM data.

relationships found in literature. The calculations are based upon the approach of *Mitchell* [1996] and were performed using an approach similar to that outlined by *Donovan* [2003]. The calculations assumed a pressure of 450 mbar, which roughly corresponds to the mean midpoint altitude of the clouds examined in the Cabauw data set.

[32] In Figure 5 it can be seen that the range of predicted Doppler velocities is roughly consistent with the ARM and Cabauw observations. It can also be seen that that habit influences the relationship between V_d and R'_{eff}, particularly for values of R'_{eff} above 75 μm. On the basis of the results of calculations such as those presented in Figure 5, it was found that for values of R'_{eff} greater than 75 μm, V_d-versus-R'_{eff} relationships corresponding to aggregate particles (i.e., see the "complex polycrystal" curve in Figure 5) generally provide a better match to the observations than relationships corresponding to nonaggregates (i.e., see the relation for "hex columns" in Figure 5). However, given the scatter of the observations and the nonunique character of the V_d-versus-R'_{eff} relationship, it is not possible to comment further here on the crystal habits that were present over the Cabauw and ARM sites.

[33] We can conclude that close agreement between the V_d-versus-R'_{eff} relationships observed at both ARM and Cabauw sites (Figure 4) is consistent with the range of habits encountered over both sites being at least not too dissimilar. Moreover, the agreement between the V_d-versus-R'_{eff} relationships observed at both ARM and Cabauw sites indicates that it is very likely that there is no important technical problem (for example, radar calibration issues) present that would prevent a valid comparison of the results found at both sites.

[34] In Figure 6 the cumulative probability of occurrence of R'_{eff} as a function of temperature for the Cabauw data is

presented. The width of the distribution obtained at the ARM site is comparable to those retrieved at Cabauw (error bars). The mean R'_{eff} in each temperature bin (3°C) is higher for the ARM site (dashed line) compared to the mean observed at Cabauw (solid line), with a difference larger than the error in the mean $R'_{eff}(T)$ of approximately 10–20%. Second, the results show that there are particles observed at lower temperatures at the former site. This was to be expected from looking at the cloud occurrence shown in Figure 2. At the ARM site the clouds are observed up to 16 km, whereas the highest Cabauw measurements reach altitudes of 12 km, both due to the limitations given by the radar and ceilometer and due to the lack of clouds. The $R'_{eff}(T)$ relationships exist; however, this comparison indicates that the relationships are local. That is, a parameterization based on the ARM data will not fit the data obtained at Cabauw or Chilbolton and is therefore not usable as a global parameterization.

[35] When comparing R'_{eff} to temperature, effectively R'_{eff} is compared to the height of the clouds at the different sites and not only the influence of the temperature on the microphysics, e.g., coagulation of particles or freezing onto particle seeds. In order to use a more cloud-geometry-related criterion, Figure 7 shows the relationship between R'_{eff} and depth into the cloud seen from cloud top ($Z_t - Z$). Even though the distribution is wide, the mean values for the two sites are very similar for depth up to 3 km. The two curves diverge for clouds with a depth greater than 3 km. In Figure 3 it was previously shown that at the Cabauw site the clouds reach thicknesses up to a maximum of 4.5 km and that any cloud thickness beyond 3 km lies in the tail of the distribution. This is different from the ARM site, where thicknesses of up to 6 km have been measured. The
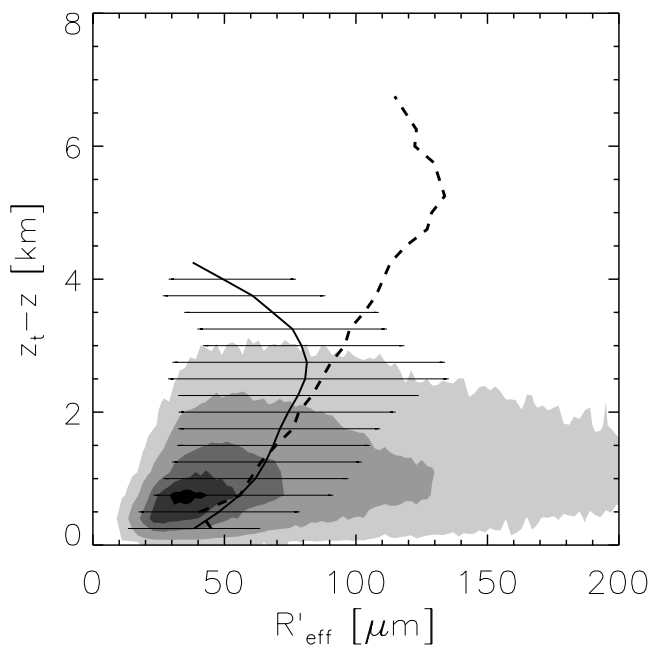

Figure 7. Cumulative probability of occurrence of the particle size (R'_{eff}) to the depth in the cloud seen from cloud top, where 0.0 stands for cloud top. The greyscale and annotations follow the same scheme as in Figure 4. The dashed line shows the mean particle size for the ARM data.
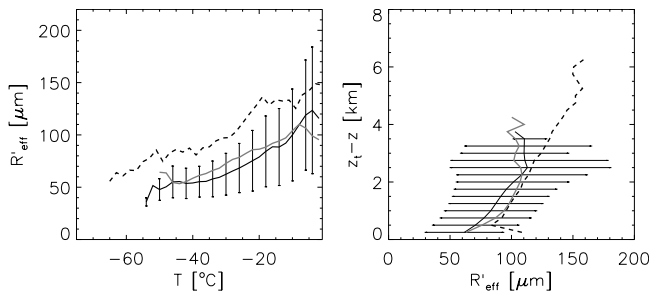
Figure 8. Results for the mean particle size (R'_{eff}) versus (left) temperature and (right) depth into cloud. The results are derived with a lower limit to the radar reflectivities (Z_e) of −20 dBZ. The solid black lines show Cabauw, the solid grey lines show Chilbolton, and the dashed lines show the ARM results. The error bars indicate the width of the distribution. Note the apparent increase of $R'_{\text{eff}}(T)$ and $R'_{\text{eff}}(Z_t - Z)$ compared to Fgures 6 and 7 due to the lower limit imposed on Z_e.

divergence of the two means could therefore well come from the difference in statistics in these thick clouds. The relation of $R'_{\text{eff}}(\Delta Z_t)$ is studied in more detail in section 6.

5.2.2. $Z_e > -20$ dBZ

[36] Because of the radar issues described in section 3 it was not possible to use the radar data below −20 dBZ for the Chilbolton site. This has a profound influence on the derived mean particle sizes. A detailed calculation of the precise influence of a lower sensitivity limit to the radar reflectivity data is presented in Appendix A. This analysis shows that when performing a direct comparison between different sites or instruments, the worst configuration has to be used to compare the data in a consistent way. In this case, this means that the radar data of the ARM and Cabauw sites have to be limited to those observations with $Z_e > -20$ dBZ (Figure 8). The results obtained at Cabauw and Chilbolton are similar to each other, which is not surprising looking at their spatial coordinates and the cloud height statistics (Figure 2). Similar results are reached when comparing R'_{eff} to the depth into the cloud. Note that in both cases the widths of the distributions are greater than shown in the cases where all radar data can be used (Figures 6 and 7).

Table 2a. IWC-Versus-Temperature Relation for Different Ice Crystal Habits, Taken From *Mitchell* [1996] and *Mitchell et al.* [1996] Except When Indicated, With the Same Particle Size Distribution[a]

Ice Habit	ARM		Cabauw	
	a	b	a	b
A_c-binned (F)[b]	0.045	0.032	0.023	0.005
D_m-binned (BF)[c]	0.036	0.027	0.022	0.003
Bullet rosettes	0.039	0.042	0.016	0.013
Columns and rosettes	0.059	0.045	0.022	0.017
Compact polycrystals	0.025	0.034	0.012	0.007
Complex polycrystals	0.030	0.035	0.014	0.008
Hex columns	0.054	0.039	0.023	0.010

[a]IWC in units of g m^{-3}, and temperature in units of °C. The fits to the data are given as IWC = ae^{bT}. See Table 2b for fits from literature presented in Figure 12.
[b]From *Francis et al.* [1998].
[c]From *Brown and Francis* [1995].

Table 2b. Fits From Literature Presented in Figure 12[a]

	a	b	c
IWC without small part[b]	0.114	0.054	
IWC with small part[b]	0.124	0.038	
IWC[c]	0.00819	0.041	
IWC[d]	2.89×10^{-6}	5.69×10^{-4}	0.0269

[a]The fits to the data are given as IWC = ae^{bT} or IWC = $aT^2bT + c$.
[b]From *Boudala et al.* [2002].
[c]From *Stephens et al.* [1990].
[d]From *Wang and Sassen* [2002].

5.2.3. Ice Water Content

[37] The ice water content (IWC) is an important ice cloud characteristic variable. As described by *Donovan and van Lammeren* [2002], the lidar/radar algorithm calculates the IWC′, which is related to IWC by IWC = IWC′ · R_{eff}/R'_{eff}. This means that IWC′, similar to R'_{eff}, is directly related to the observed quantities but depends implicitly on the habit and the particle size distribution.

[38] In this section, the complex polycrystal ice habit assumption is adopted when using IWC. For comparison, IWC(T) fits for other habits are presented in Tables 2a and 2b. In order to gain some insight into the range of derived ice water content values, the probability distribution functions of IWC′ and IWC are given in Figure 9 for the Cabauw and ARM sites. The IWC′ and IWC determined at the Cabauw site show a slightly broader distribution and are shifted by a small factor (∼2−3) compared to the ARM site. For $Z_e > -20$ dBZ the distributions at Cabauw and Chilbolton are similar.

[39] In many places in the literature the IWC has been correlated to the radar reflectivity (e.g., *Sassen et al.* [2002] (see their Table 1 for an overview) and *Norquist and D'Entremont* [2003]). Before comparing the results calculated in this work to the literature, first the IWC′ is compared to Z_e for the Cabauw and ARM sites in Figure 10. The two IWC′-versus-Z_e distributions have very similar fits (IWC′ = 0.098 $Z_e^{0.347}$ and IWC′ = 0.153 $Z_e^{0.364}$ for ARM and Cabauw, respectively) as well as distribution widths.

[40] After converting IWC′ to IWC, it is not surprising that the IWC-versus-Z_e (Figure 11) relationships are very similar for both sites. The fits to the results (IWC ∝ $Z_e^{0.32}$) are less steep compared to results found in the literature (between 0.483 and 0.83 [*Sassen et al.*, 2002, Table 1]). The region in which 30% of all points lie has a steeper slope compared to the mean of all points, more equal to the values found in the literature.
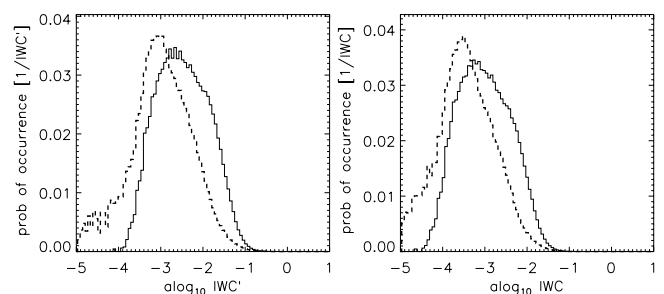

Figure 9. Probability distribution function of (left) IWC′ and (right) IWC for the ARM (dashed lines) and Cabauw (solid lines) sites.
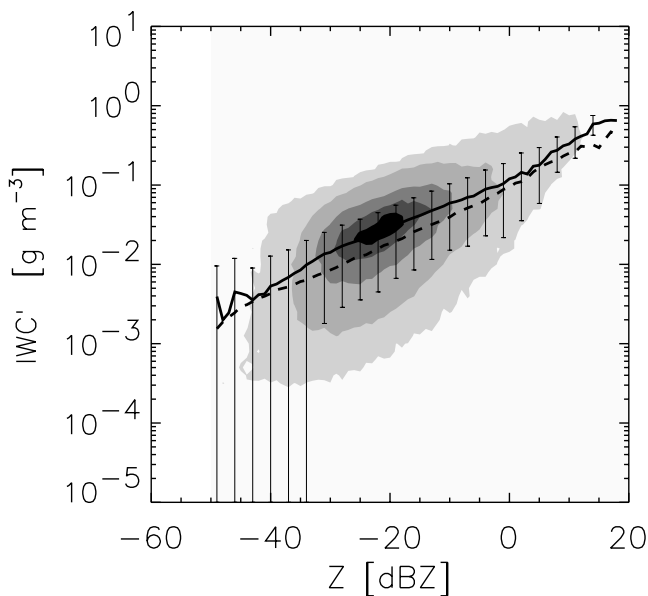
Figure 10. Cumulative probability of occurrences of the ice water content (IWC′) as a function of radar reflectivity (Z_e). The greyscale shows the 10 (darkest), 30, 60, 90 and 99% probability of occurrence using linear scaling in log space at Cabauw. The solid line shows the corresponding mean IWC′ at each radar reflectivity, with the error bars indicating the width of the distribution. The dashed line is the mean IWC′ observed at the ARM site.
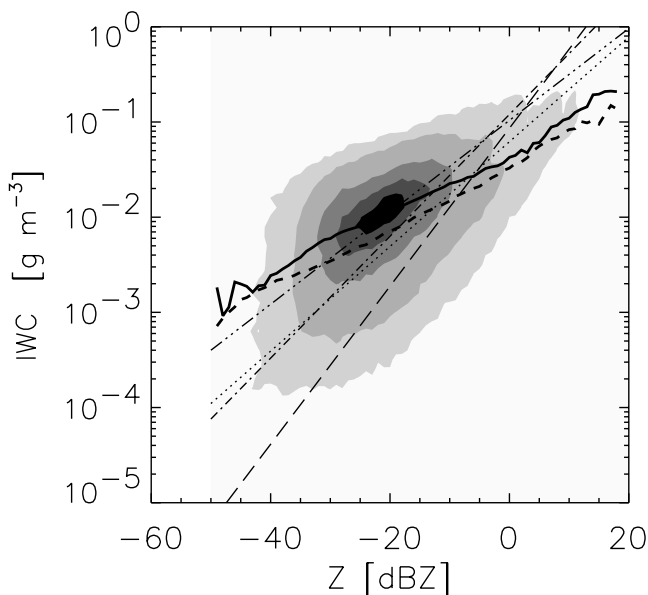
[41] One of the reasons for this difference in the mean could be the assumption of a single habit and particle size distribution. On the other hand, this work has the benefit of high sensitivity and a large data set, giving good statistics, whereas results based on in situ data are limited in time and sensitivity. A more thorough examination of this will be presented in future work.

[42] IWC has been parameterized previously with temperature for Earth climate modeling [e.g., *Stephens et al.*, 1990; *Boudala et al.*, 2002; *Wang and Sassen*, 2002]. In Figure 12 the *T*-versus-IWC distributions are shown for both ARM and Cabauw sites using the complex polycrystal ice habit. Overplotted on these are the results from the three papers mentioned above.

[43] The results of *Stephens et al.* [1990] and *Boudala et al.* [2002], both using in situ data, overlap the observed values presented but either have a larger slope or lie above the mean IWC(*T*) relationship. The points used by *Boudala et al.* [2002] to derive their fit are given as well. This serves no other purpose than to show the range and scatter of the data points obtained when using in situ data compared to active remote sensing. The results from *Wang and Sassen* [2002] were derived from data observed at the same ARM site, during the same period of time. The data, however, were obtained using a different lidar, the CART Raman lidar, at 0.355 μm. The good comparison of the two

Figure 11. Cumulative probability of occurrences of the ice water content (IWC) of the complex polycrystal habit as a function of radar reflectivity (Z_e). The greyscale and annotations follow the same scheme as in Figure 10. The thick solid line represents the mean IWC at Cabauw, and the thick dashed line represents the mean IWC at the ARM site. The thin lines are fits taken from *Sassen et al.* [2002] (their Table 1, entry 5 (long-dashed line) and entry 6 (triple-dot-dashed line)), *Matrosov et al.* [2003] (dot-dashed line) and *Norquist and D'Entremont* [2003] (dotted line).
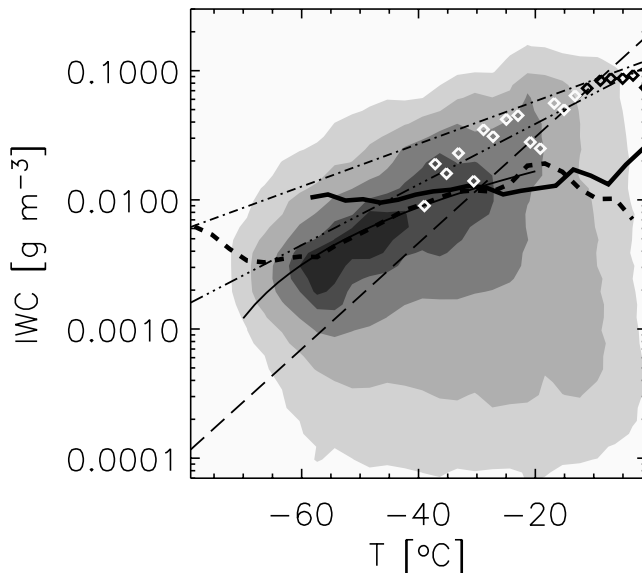

Figure 12. Cumulative probability of occurrence of the ice water content (IWC) at each temperature, for complex polycrystal ice at the ARM site. The thick dashed line shows the mean IWC (g m^{-3}) at each temperature (°C), and the thick solid line shows the mean IWC as observed at Cabauw. Overplotted are data taken from *Boudala et al.* [2002], with the dot-dashed line being the fit from their Table II (no small particles) and the diamonds and triple-dot-dashed line being the fit from their Table III (including small particles). The different shades of the diamonds are used for contrast only. The thin long-dashed line is taken from *Stephens et al.* [1990], and the thin solid line shows the fit after *Wang and Sassen* [2002].
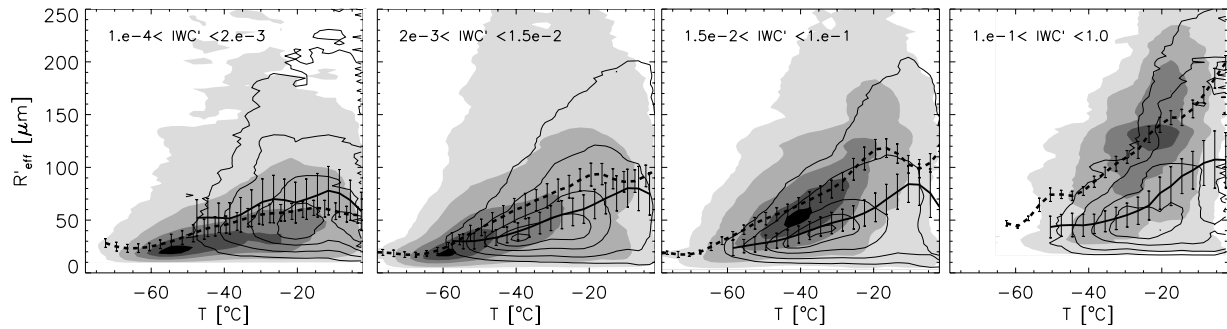
Figure 13. Cumulative probability of occurrence for R'_{eff} to T for different ice water content (g m^{-3}) bins, noted in each panel. The contour levels (greyscale for ARM and contours for Cabauw) follow the same scheme as in Figure 4. The dashed lines show the mean $R'_{eff}(T)$ observed at ARM, and the solid lines show that retrieved at the Cabauw site. The error bars denote the error in the mean.

different methods and instruments gives confidence in the IWC values calculated.

[44] The results for a few other habits are presented in Tables 2a and 2b. In all cases the offsets of the function at $T = 0°C$ are different for the ARM and Cabauw sites, even though the means overlap each other within the error bars for a large part. In the case of Cabauw (and Chilbolton for $Z_e > -20$ dBZ) the slope of the function is smaller, and in some cases there is no dependence of IWC on temperature. The different habit fits found in the ARM site results have slopes close to the values found by *Boudala et al.* [2002] but have different offsets. The *Wang and Sassen* [2002] results are roughly consistent with the ARM and Cabauw results.

[45] Now that the $R'_{eff}(T)$ and the IWC′/IWC temperature relationships have been studied, a combination of the three variables can be made. *Donovan and van Lammeren* [2002] and *Donovan* [2003] showed that the R'_{eff}-versus-T relationship depended on the IWC′ range considered. This result suggested a possible parameterization of $R'_{eff}(T, IWC)$ and could therefore be of great importance for modeling. In Figure 13 the same IWC′ binning as used by *Donovan* [2003] is used for the results from the Cabauw site. The comparison between the two sites is good for very low IWC′ ($10^{-4} < IWC' < 2 \times 10^{-3}$); however, the mean $R'_{eff}(T)$ relationships deviate more and more for higher IWC′. For $Z_e > -20$ dBZ the Chilbolton and Cabauw sites again have results within the error bars. This comparison indicates that there will most likely not be a global $R'_{eff}(T, IWC)$, and therefore $R_{eff}(T, IWC)$ parameterization is not possible.

5.2.4. Visible Extinction

[46] The visible extinction profile is the most important parameter in determining a cloud's radiative impact. Lidars, being optical instruments, are well suited for determining extinction profiles. However, lidars can often be attenuated before full cloud penetration is achieved. Since radars can often obtain useful signal in clouds where the lidar signal is extinguished, it is useful to consider how accurate extinction may be linked to radar reflectivity alone.

[47] In Figure 14 the visible extinction is plotted versus the radar reflectivity. The Cabauw and ARM sites have similar distributions, with a slightly lower mean α for the latter site. The higher end of the distribution is limited by

the maximum optical thickness detectable with a vertical resolution of roughly 100 m.

[48] These results show a shallower slope, compared to results from *Hogan et al.* [2003, p. 2124] using EUCREX data for midlatitude cirrus and *Matrosov et al.* [2003] for ice clouds. In both works, in situ data are used to derive the extinction, assuming relationships of particle mass versus size and cross-sectional area, whereas the extinction in this work is directly related to the derivative of the lidar signal without any ice habit assumptions.

[49] The difference between the data sets could be caused by several things. First of all, data obtained during a
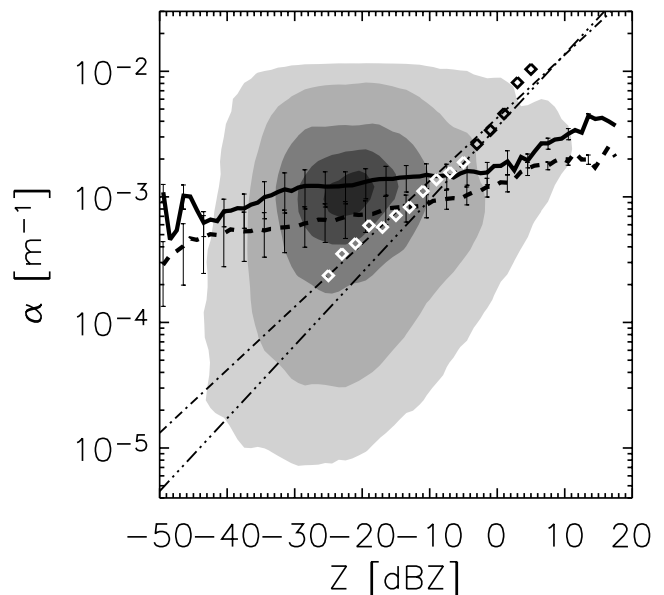

Figure 14. Cumulative probability of occurrence of the extinction (α) as a function of radar reflectivity (Z_e) using Cabauw data. The greyscale and lines follow the same scheme as in Figure 10. The error bars show the error in the mean. The diamonds and dot-dashed line show the results obtained by *Hogan et al.* [2003, p. 2124], and the triple-dot-dashed line shows the results from *Matrosov et al.* [2003]. The different shades of the diamonds are used for contrast only.
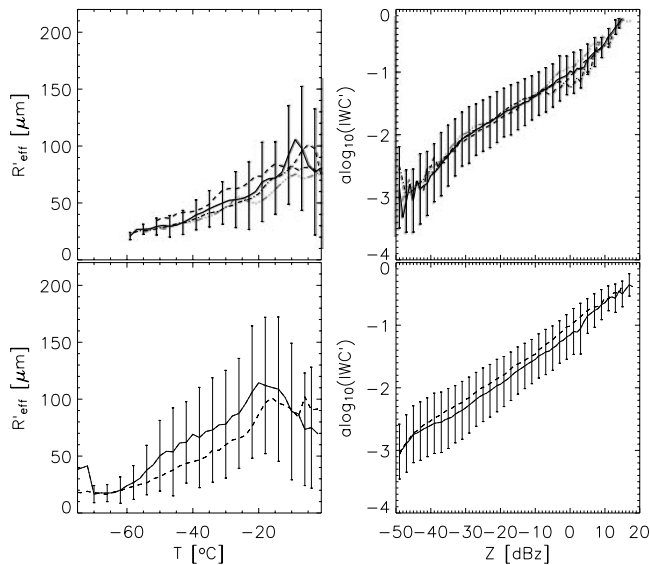
Figure 15. (left) Mean calculated effective radius (R'_{eff}) at each temperature and (right) mean IWC′ as a function of radar reflectivity, for the four meteorological seasons: winter (solid line), spring (dash-dotted line), summer (dashed line), and autumn (dash-triple-dotted line). Both the data for the Cabauw (top panels) and the ARM site (bottom panels) are shown. The error bars indicate the width of the distribution.

campaign are taken only during a limited period of time, while the results presented here are the means over a long period of time. Second, the fitted results could be a combination of data observed at different positions on Earth looking at different types of cirrus, while the data analyzed in this paper are observed at the same site.

5.3. Seasonal Dependence

[50] The results presented in the previous sections are based on a large data set spanning more than 1 year. It is therefore important to recognize whether there are time dependencies that may have been overlooked. In Figure 15 the seasonal dependence of the Cabauw and ARM sites are shown. In the case of Cabauw, observations are made continuously over a long period of time, and a comparison can be performed for the four (meteorological) seasons. The data available for the ARM site are predominately taken in the winter and summer, and consequently, the results are shown only for these two seasons. Both the $R'_{eff}(T)$ and IWC′(Z) relationships are plotted for the different seasons. In the latter case the seasonal differences are within the error in the mean for both sites, showing the robustness of this relationship. For Cabauw there is no difference in the $R'_{eff}(T)$ relation for the four seasons. The ARM data show a small dependence between the winter and summer seasons on the order of the error in the mean estimate of $\approx 10-20\%$. Whether the difference in the results presented above is truly due to ice cloud differences or due to statistics needs to be investigated in the future with larger data sets. The results of *Wang and Sassen* [2002] showed that there is hardly any difference between the summer and winter seasons as well. These two studies give us confidence that there is no seasonal dependence and that all the available

data can be used to derive microphysical parameters valid for the entire year at both positions.

6. Particle Size Cloud Depth Dependence

[51] In section 5.2.1 it was found that the mean effective particle sizes to depth into cloud from cloud top showed a similar behavior for the Cabauw, ARM and Chilbolton sites. This observation warrants further investigation. The results so far are based upon all cloud thicknesses within the data set and showed a discrepancy for depths >3 km. Accordingly, the distributions have been separated into four total cloud thickness regimes (separated at each 1.5 km, Figure 16), for which the mean particle sizes to depth into the clouds are compared.

[52] For the ARM site (Figure 16), it can be seen that the mean particle sizes just below cloud top are roughly the same ($R'_{eff} \approx 40-50$ μm) for all thicknesses and grow to larger particle sizes deeper in the clouds. The geometrically thicker clouds show a more rapid increase of the mean particle size deeper in the clouds.

[53] The profiles show more or less a parabolic profile like that suggested by *Khvorostyanov and Sassen* [1998] and predicted in numerical calculations by *Liu et al.* [2003]. More interesting is that the mean profiles observed at the ARM and Cabauw sites are the same within the error bars for the three cloud thickness regimes adopted.

[54] The $R'_{eff}(T)$ was strongly influenced by the IWC′ regime. To check for the influence of IWC′ on the $R'_{eff}(\Delta Z_t)$ relationship, they were recalculated for the IWC′ bins used in the $R'_{eff}(T, IWC)$ test case. The results for both ARM and Cabauw data are given in Figure 17. In all except for the lowest IWC′ bin, the two mean $R'_{eff}(\Delta Z_t)$ relationships overlap, and even the distributions look very similar for the 4 km closest to cloud top. The mean in each of the IWC′ bins shifts to larger R'_{eff} for larger IWC′ values.

[55] The profiles shown in Figures 13 and 17 can be explained when considering particle aggregation. Though a detailed discussion of the particle size growth is beyond the scope of this paper, a few remarks are made here. *Mitchell* [1991] showed that the increase in particle size depends mostly on the aggregation efficiency (E_a), the IWC and the dispersion in fall velocities. This would mean that for a larger IWC the particle sizes should increase. This is exactly what is shown from left to right in Figures 13 and 17, with the mean R'_{eff} increasing in larger IWC′ bins. The earlier mentioned problem in the lowest IWC′ bin (Figure 17; $10^{-4} < IWC' < 2 \times 10^{-3}$), where the mean particle size relationships between the two sites did not overlap, can be explained in the same way. Looking at the two observed IWC′ histograms (Figure 9; left panel), the ARM site has a lower mean IWC′ in the $10^{-4} < IWC' < 2 \times 10^{-3}$ bin, which would result in a mean lower particle size for the ARM site.

[56] When looking at Figure 16, one can see that the particles aggregate to bigger sizes in thicker clouds. This is not surprising as particles fall through a larger parcel of air. However, when concentrating on the region just below the cloud top, the increase in particle size is larger for geometrically thicker clouds as well. This cannot be explained easily using the IWC′ argument as these are similar (≈ 0.02 g m^{-3}), within the error bars for the four thickness
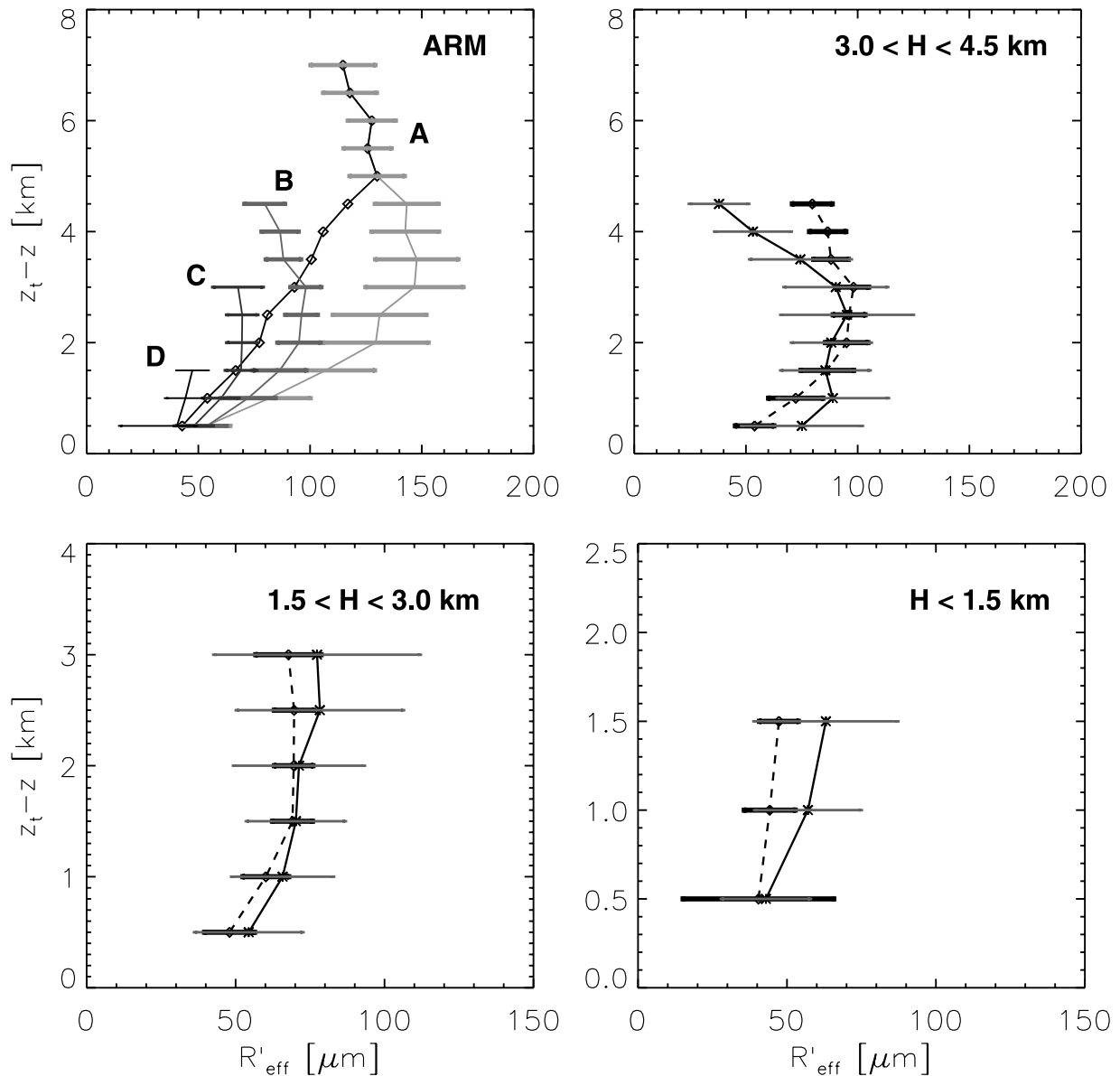
Figure 16. The top left plot shows the mean particle size at each depth for four different total cloud thickness (*H*) regimes (*H* > 4.5 (A), 3.0 < *H* < 4.5 (B), 1.5 < *H* < 3.0 (C), and *H* < 1.5 (D)) observed at the ARM site. The solid black line with diamonds is the mean particle size for the entire data set without thickness variation. In the top right plot, curve B is compared for the ARM (dashed line with diamonds) and Cabauw sites (solid line with asterisks). The thick error bars indicate the errors in the mean for the ARM, and the thin ones indicate those for the Cabauw results. The same notation is used for the lower left and lower right fgures, where curves C and D, respectively, are compared.

regimes just below cloud top. Future work using more data and thereby reducing the noise might give more insight into the behavior of these profiles.

[57] As R'_{eff} is not the parameter most directly required by climate models, the mean values of R'_{eff} found at the ARM site are converted to R_{eff}. This was done by adopting the complex polycrystal ice habit and using the particle size distribution model used by *Donovan* [2003]. Both the habit and form of the particle size distribution are needed to calculate the $\langle M^2(D)\rangle/\langle M(D)\rangle$ ratio (equation (2)).

[58] In Figure 18 the R_{eff} versus normalized cloud depth is plotted. This is the direct conversion of the top left panel

of Figure 16, using the same cloud thickness regimes, where each cloud is normalized to its cloud thickness. The figure is inverted so that cloud top is at the top of the figure and cloud bottom is at the bottom. The mean particle sizes can be described by parabolic relationships to normalized cloud depth (solid lines) for each of the cloud thickness regimes. A linear relationship seems more appropriate, though, for the $H < 1.5$ km clouds. In a future paper a parameterization for the different ice particle habits and particle size distribution will be given.

[59] If the R'_{eff} and R_{eff} relationships presented can be validated at more climatic different locations, a global
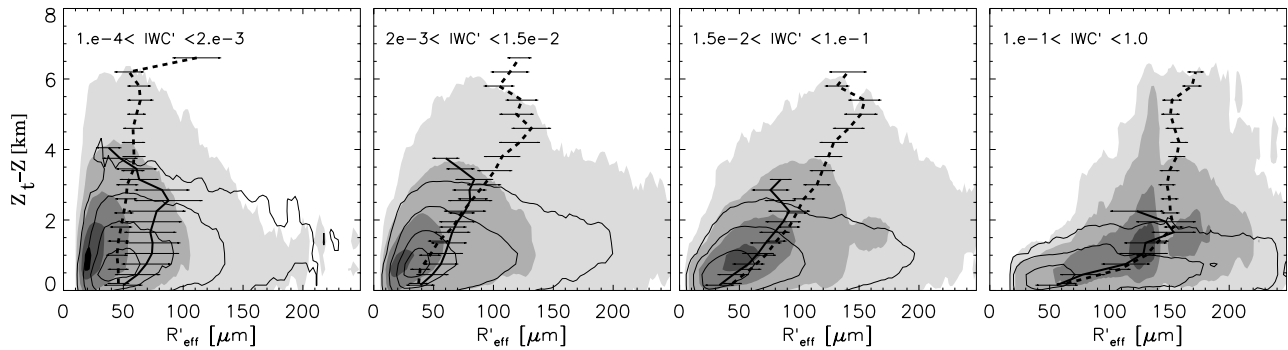
Figure 17. Cumulative probability of occurrence for R'_{eff} to $Z_t - Z$ for different ice water content (g m^{-3}) bins, noted in each panel, using the exact same bins as in Figure 13. The contour levels (greyscale for ARM and contours for Cabauw) follow the same scheme as in Figure 4. The dashed lines show the mean $R'_{eff}(Z_t - Z)$ observed at ARM, and the solid lines show that retrieved at the Cabauw site. The error bars denote the error in the mean.

parameterization of particle sizes can be constructed depending on the depth into the cloud (ΔZ_t) and total thickness (H) of the cloud.

[60] A thorough investigation of this will be possible using Cloudsat and Calipso, the first lidar-radar combination in space, which should fly in 2005.

7. Conclusions

[61] A comparison of the microphysical properties of ice clouds is made for three different sites, Cabauw (Netherlands), ARM-SGP (United States), and Chilbolton (United Kingdom), using active remote sensing data. Using lidar and radar the effective radii, extinction and ice water content are derived and correlated to each other, temperature, radar reflectivity and depth into the cloud. The ice clouds used in this work form a subset of all ice clouds as only clouds up to an optical depth of $\tau \sim 4$ are taken into account.

[62] The most important conclusions can be summarized as follows: (1) The relationship between the mean Doppler velocity and the mean derived particle sizes (R'_{eff}) is the same for all three sites. (2) Ice water content (IWC$'$ and IWC) and radar reflectivity have a very similar relationship for the three sites. (3) Within the sensitivity studies performed in this work it is not possible to construct a $R'_{eff}(T)$ or $R'_{eff}(T, IWC)$ parameterization that applies to both the ARM-SGP site and the two European sites. This implies that a global description of R_{eff} as a function of T and IWC is not possible. (4) The mean ice water content (IWC) to temperature relation shows similar results for the ARM and Cabauw sites. (5) The particle size (R'_{eff}) versus depth into cloud from cloud top ($Z_t - Z = \Delta Z_t$) relationship shows very similar results for the three sites. The $R'_{eff}(\Delta Z_t)$ profiles show increasing particle sizes for thicker (H) clouds. Binning by IWC$'$ reveals an identical behavior for the different sites. This behavior may form the basis for a global parameterization of ice microphysical properties to include in GCMs. (6) No seasonal dependence is detected for the low optically thick clouds observed at Cabauw. A slight dependence might be there for the ARM site, but within the range of error. A larger data set has to be used to confirm this. (7) Future observations using satellites

(Cloudsat, Calipso and EarthCARE) should be able to confirm the above results and will result in a parameterization of R_{eff} on a global basis. The satellite results will benefit highly from their global coverage and will have no problem with detecting cloud top and a large part of the cirrus clouds from their point of view.

Appendix A. Radar Sensitivity Study

[63] The procedure used in this and previous work depends on the observed lidar and radar data. In the case of the lidar the precise calibration is not important [*Donovan*, 2003]. This is not so for the radar data, for which
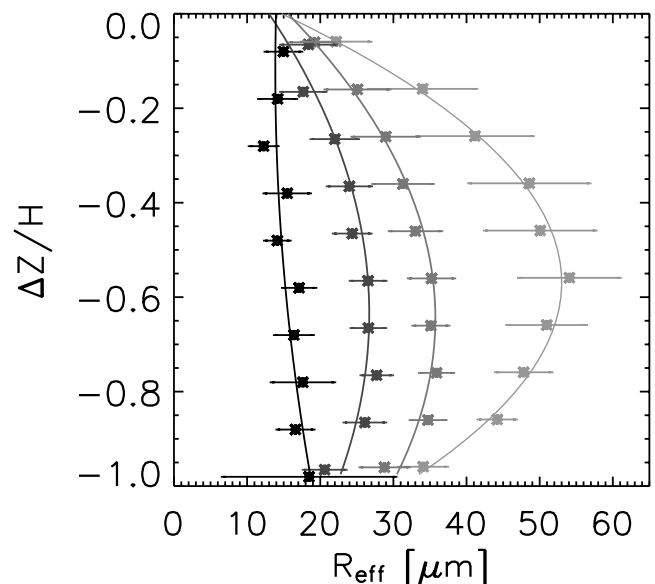

Figure 18. Mean R_{eff} versus normalized cloud depth (ΔZ (km)) seen from cloud top adopting the complex polycrystals as ice habit for four different total cloud thickness (H (km)) regimes ($H > 4.5$, $3.0 < H < 4.5$, $1.5 < H < 3.0$, and $H < 1.5$ from light grey to black points) at the ARM site. Note that cloud top is at 0 and cloud bottom is at -1. The error bars show the error in the mean, and the solid lines show a second-order polynomial fit to the data.
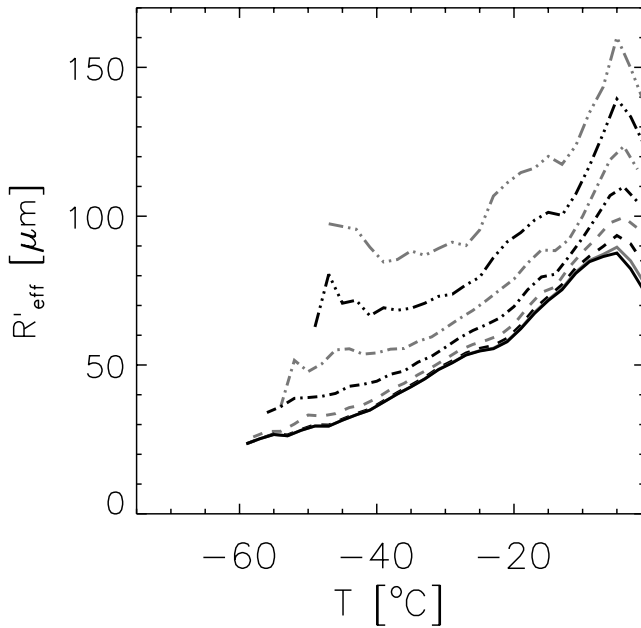
Figure A1. Influence on the $R'_{\text{eff}}(T)$ relationship due to a lower limit in radar reflectivity (Z_e). The results have lower limits as follows: -10 dBZ (dash-triple-dotted grey line), -15 dBZ (dash-triple-dotted black line), -20 dBZ (dash-dotted grey line), -25 dBZ (dash-dotted black line), -30 dBZ (dashed grey line), -35 dBZ (dashed black line), -40 dBZ (solid grey line) and -45 dBZ (solid black line).

a correct calibration is required to retrieve the correct microphysical parameters. In this work, there was the additional problem that for a large part of the time the radar signal was not valid below -20 dBZ for one of the sites. To test the influence of the radar on the retrieved parameters, the temperature dependence on the particle size is determined for different lower limits of the radar signal (Figure A1). In steps of 5 dBZ the $R'_{\text{eff}}(T)$ relationship is examined from a lower limit of -10 dBZ down to -45 dBZ. It is clear that the mean particle size is larger for a higher lower limit. Intuitively, this is easy to understand as in the Rayleigh regime $Z_e \propto r^6$. When Z_e has a lower limit, there is also a lower limit to the particle size. The mean particle size relation, however, remains the same (within the error bars) for $Z_e < -35$ dBZ. To conclude, the derived mean particle sizes for the Cabauw and ARM sites have converged with respect to the sensitivity of the observed radar signal. The Chilbolton results have not converged and cannot be directly used in a comparison with the other two sites. To do this, the radar sensitivity used for the Cabauw and ARM sites has to be raised to -20 dBZ.

Appendix B. Lidar Sensitivity Study

[64] There is a large difference in power output between the ceilometers and the Micropulse Lidar, and it is therefore of importance to make sure that any difference in the retrieved parameters is not due to differences in the instruments. The derivation of the microphysical parameters does not depend on an accurate absolute calibration of the lidar. The local extinction can be derived from the derivative of the signal while accounting for the effects of multiple

scattering. What is important is to check for differences in the "true" lidar signal, on the basis of the observed extinctions at the different sites. The difference in power and telescope opening angle has a second effect as the CT-75K is influenced by daytime, resulting in larger errors compared to nighttime and thereby missing clouds that would have been seen during nighttime. This is less the case for the stronger MPL with the small field of view compared to the ceilometer, and this might influence the derived mean particle size. In Figure B1 the normalized probability of occurrence of cloud pixels at a certain time of day is presented for the ARM and Cabauw sites. At the latter site it is clear that there are a relatively small number of fully visible clouds during daytime (in between 0500 and 1700 UT) compared to the ARM site, which has a more evenly spread distribution. To make sure that this artificially introduced sampling error does not affect the main conclusions drawn in this work, the R'_{eff}-versus-temperature relation is calculated for "nighttime" only (1700–0500 UT, Figure B1). The bias introduced has no effect on the mean particle size at each temperature. The direct effect of the difference in power can be seen using the lidar equation. The lidar equation expressed in units of power can be written as

$$P_{ss}(z) = C_{\text{lid}} \frac{\beta_{\text{lid}}(z)}{z^2} \exp\left[-2\int_{z_o}^{z} \alpha(z')dz'\right], \quad (\text{B1})$$

where α is the extinction coefficient at the lidar wavelength, β_{lid} is the corresponding backscatter coefficient and P_{ss} is the power. C_{lid} is the calibration constant concerning the lidar power and telescope and other variables not due to the clouds. In this case it is assumed that $\beta_{\text{lid}} = \alpha/25$, and the lidar equation is calculated for each cloud pixel using

$$P'_{ss}(z) = \frac{\alpha(z)}{25z^2} \exp\left[-2\int_{z_o}^{z} \alpha(z')dz'\right], \quad (\text{B2})$$

where $P'_{ss}(z)$ is the "true" single-scattering lidar signal. In Figure B2, $P'_{ss}(z)$ is plotted against height for both Cabauw and ARM sites. As the clouds at ARM occur at higher
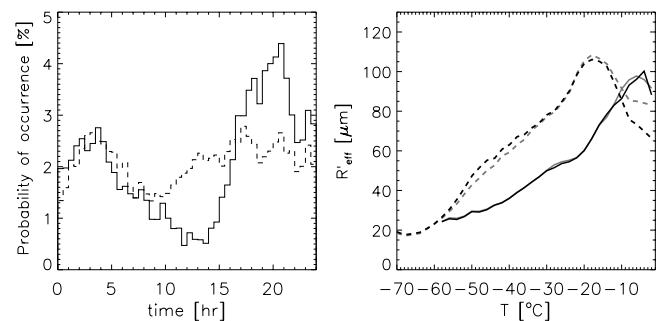

Figure B1. (left) Normalized probability of occurrence of cloud pixels at a certain time of day for Cabauw (solid line) and ARM (dashed line) with a bin size of half an hour. (right) Influence of the entire data set (Cabauw, grey solid line; ARM, grey dashed line) compared to the data only observed at night (in between 1700 and 0500 UT; Cabauw, black solid line; ARM, black dashed line.)
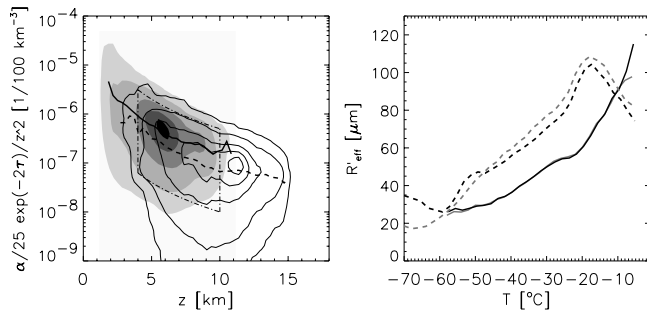
Figure B2. (left) Lidar signal plotted versus height. The greyscale and solid line (mean) are used for Cabauw data, and the contour lines and dashed line (mean) are used for the ARM data. The dash-dotted "box" denotes the area for which the effect of the difference in lidar power is probed. (right) $R'_{\text{eff}}(T)$ relation for ARM (dashed lines) and Cabauw (solid lines). The grey lines show the results for the entire data set, and the solid lines show the results when only the dash-dotted box from the left panel is taken into account.

altitudes, the maximum signal is lower than at the Cabauw site. The two sites do seem to have the same slope with roughly a factor of 2 in offset. The ARM lidar, however, is capable of detecting at least an order lower values of $P'_{ss}(z)$. To check for the sensitivity on the derived mean values, two checks are performed. First a part of the lidar signal height space is bounded by taking the area in between $1 \times e^{-6}/z^2 < P'_{ss}(z) < 5 \times e^{-5}/z^2$ and $5 < z < 10$ (see Figure B2). This area is populated by both the ARM as well as the Cabauw data and should give an unbiased comparison of the two sites. The mean particle size at the ARM site does drop slightly (Figure B2, right panel), but the shift falls within the error of the mean (10–20%) and does not bring it on top of the Cabauw results. The same conclusion holds when both the effect of the difference in lidar power and the time effect are taken into account. Therefore even though the precise $R'_{\text{eff}}(T)$ relation can differ by up to 10–20% (same as the estimate of the error), the two sites show a different $R'_{\text{eff}}(T)$ relationship. In comparison, the $R'_{\text{eff}}(\Delta Z_t)$ relationship shows the same results as presented in Figure 16 when taking these effects into account.

Appendix C. Influence of Different Particle Habits

[65] In this work, as soon as R_{eff} or IWC is used (instead of R'_{eff} or IWC'), it is assumed that a single habit holds for the entire period at every height and all possible weather conditions. This is of course highly unlikely. However, in order to derive parameterizations for the particle sizes at a certain location, any other approach is not feasible at the moment. The error introduced by assuming a habit is shown here, where the R_{eff} relationships are shown for several different particle habits for a bimodal size distribution with a constant ratio in total scatterers (N) between the large and small modes. In this paper, the exact same relationships as used by *Donovan* [2003] are taken. In Figure C1 the $R_{\text{eff}}/R'_{\text{eff}}$ to R'_{eff} is shown for several habits. The habit relationships were taken from literature (see Tables 2a and 2b for references).
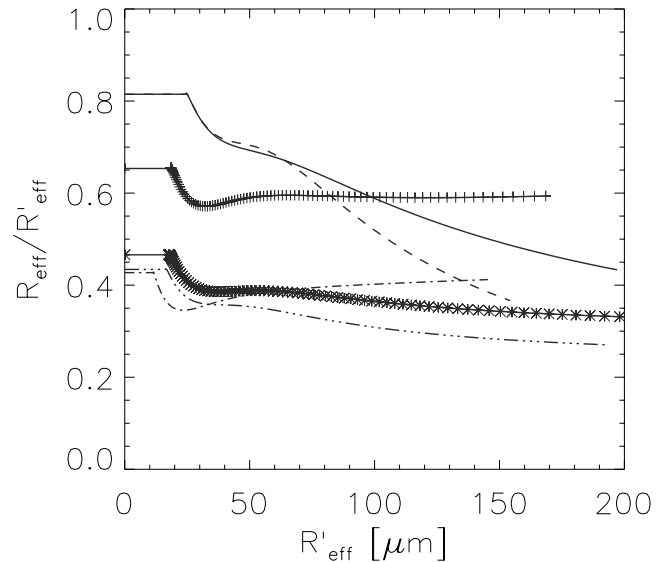

Figure C1. $R_{\text{eff}}/R'_{\text{eff}}$ fraction to R'_{eff} for the different habits using a bimodal distribution. The solid line and the dashed line are taken from *Francis et al.* [1998] and *Brown and Francis* [1995], where the former used A_c binning and the latter used D_m binning. The dot-dashed line represents bullet rosettes, and the dash-triple dotted line represents the compact polycrystals. The solid line with stars shows the complex polycrystals, and finally, the solid line with pluses shows the hex columns.
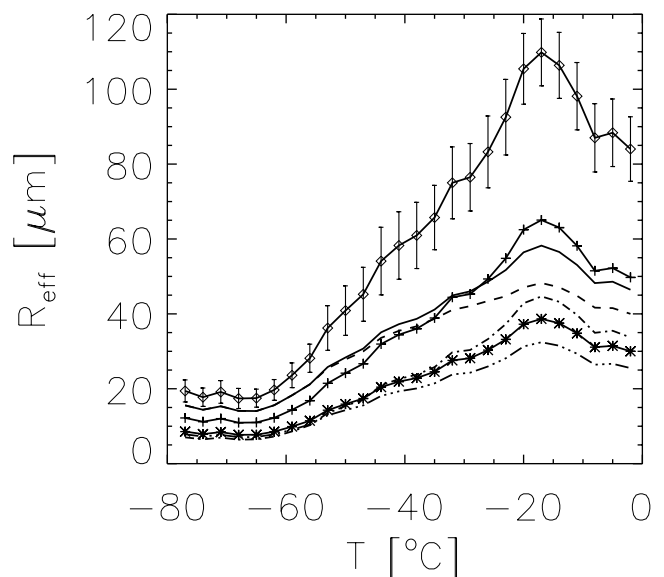

Figure C2. Ice habit influence on the R_{eff}-versus-T relation for the ARM data set. The solid line with diamonds and error bars shows the R'_{eff} from which the R_{eff} relations are derived. The error bars are given by the error in the mean. The standard deviation of the population is a lot larger and can reach up to 40 μm. The solid line and the dashed line are taken from *Francis et al.* [1998] and *Brown and Francis* [1995], where the former used A_c binning and the latter used D_m binning. The dot-dashed line represents bullet rosettes, and the dash-triple-dotted line represents compact polycrystals. The solid line with stars shows the complex polycrystals, and finally, the solid line with pluses shows the hex columns.

[66] As seen in the figure, there are roughly three types of habits. The two BF and F have a high ratio for small particles and drop to $0.3-0.4$ for larger particles. The polycrystals and bullet rosette ratios stay roughly constant around 0.4, and the hex columns are roughly constant around 0.6.

[67] Using this to see the effect this has on the derived R_{eff} to temperature relationship, Figure C2 shows the results for the ARM site for the different habits. The R'_{eff} relation is also presented for reference in the plot.

[68] As these comparisons are performed by changing the ice habit only and not a combination of habit and the size distribution, a more detailed comparison has to be performed in the future. This is a too elaborate computation for now and will be presented in a coming paper.

References

Arking, A. (1991), The radiative effects of clouds and their impact on climate, *Bull. Am. Meteteorol. Soc.*, *72*, 795–953.

Boudala, F. S., G. A. Isaac, Q. Fu, and S. G. Cober (2002), Parameterization of effective ice particle size for high latitude clouds, *Int. J. Climatol.*, *22*, 1267–1284.

Brown, P. R. A., and P. N. Francis (1995), Improved measurements of the ice water content in cirrus using a total-water probe, *J. Atmos. Oceanic Technol.*, *12*, 410–414.

Donovan, D. P. (2003), Ice-cloud effective particle size parameterization based on combined lidar, radar reflectivity, and mean Doppler velocity measurements, *J. Geophys. Res.*, *108*(D18), 4573, doi:10.1029/2003JD003469.

Donovan, D. P., and A. C. A. P. van Lammeren (2001), Cloud effective particle size and water content profile retrievals using combined lidar and radar observations: 1. Theory and examples, *J. Geophys. Res.*, *106*, 27,425–27,448.

Donovan, D. P., and A. C. A. P. van Lammeren (2002), First ice cloud effective particle size parameterization based on combined lidar and radar data, *Geophys. Res. Lett.*, *29*(1), 1006, doi:10.1029/2001GL013731.

Donovan, D. P., et al. (2001), Cloud effective particle size and water content profile retrievals using combined lidar and radar observations: 2. Comparison with IR radiometer and in situ measurements of ice clouds, *J. Geophys. Res.*, *106*, 27,449–27,464.

Eloranta, E. W. (1998), Practical model for the calculation of multiply scattered lidar returns, *Appl. Opt.*, *37*, 2464–2472.

Francis, P. N., P. Hignett, and A. Macke (1998), The retrieval of cirrus cloud properties from aircraft multi-spectral reflectance measurements during EUCREX '93, *Q. J. R. Meteorol. Soc.*, *124*, 1273–1291.

Garrett, T. J., H. Gerber, D. G. Baumgardner, C. H. Twohy, and E. M. Weinstock (2003), Small, highly reflective ice crystals in low-latitude cirrus, *Geophys. Res. Lett.*, *30*(21), 2132, doi:10.1029/2003GL018153.

Heymsfield, A. J. (2003), Properties of tropical and midlatitude ice cloud particle ensembles. Part II: Applictaions for mesoscale and climate models, *J. Atmos. Sci.*, *60*, 2592–2611, doi:10.1175/1520-0469(2003)060.

Heymsfield, A. J., and J. Iaquinta (2000), Cirrus crystal terminal velocities, *J. Atmos. Sci.*, *57*, 916–938.

Heymsfield, A. J., and G. M. McFarquhar (2002), Mid-latitude and tropical cirrus, in *Cirrus*, edited by D. K. Lynch et al., pp. 78–101, Oxford Univ. Press, New York.

Hogan, R. J., A. J. Illingworth, E. J. O'Connor, and J. P. V. Poiares Baptista (2003), Characteristics of mixed-phase clouds. Part II: A climatology from ground-based lidar, *Q. J. R. Meteorol. Soc.*, *129*, 2117–2134.

Khvorostyanov, V. I., and K. Sassen (1998), Cirrus cloud simulation using explicit microphysics and radiation. Part II: Microphysics, vapor and ice mass budgets, and optical and radiative properties, *J. Atmos. Sci.*, *55*, 1822–1845.

Klett, J. D. (1981), Stable analytical inversion solution for processing lidar returns, *Appl. Opt.*, *20*, 211–220.

Kristjánsson, J. E., J. M. Edwards, and D. L. Mitchell (2000), Impact of a new scheme for optical properties of ice crystals on climates of two GCMs, *J. Geophys. Res.*, *105*, 10,063–10,080.

Liu, H., P. K. Wang, and R. E. Schlesinger (2003), A numerical study of cirrus clouds. Part II: Effects of ambient temperature, stability, radiation, ice microphysics, and microdynamics on cirrus evolution, *J. Atmos. Sci.*, *60*, 1097–1119.

Matrosov, S. Y., M. D. Shupe, A. J. Heymsfield, and P. Zuidema (2003), Ice cloud optical thickness and extinction estimates from radar measurements, *J. Appl. Meteorol.*, *42*, 1584–1597.

McFarquhar, G. M., S. Iacobellis, and R. C. J. Somerville (2003), SCM simulations of tropical ice clouds using observationally based parameterizations of microphysics, *J. Clim.*, *16*, 1643–1664.

Mitchell, D. L. (1991), Evolution of snow-size spectra in cyclonic storms. Part II: Deviations from the exponential form, *J. Atmos. Sci.*, *48*, 1885–1899.

Mitchell, D. L. (1996), Use of mass- and area-dimensional power laws for determining precipitation particle terminal velocities, *J. Atmos. Sci.*, *53*, 1710–1723.

Mitchell, D. L., S. K. Chai, Y. Liu, A. J. Heymsfield, and Y. Dong (1996), Modeling cirrus clouds. Part I: Treatment of bimodal size spectra and case study analysis, *J. Atmos. Sci.*, *53*, 2952–2966.

Norquist, D. C., and R. P. D'Entremont (2003), Analysis and prediction of cirrus-top altitude and ice water path in a mesoscale area, *J. Appl. Meteorol.*, *42*, 1092–1106.

Quante, M., and D. O. C. Starr (2002), Dynamical processes in cirrus clouds, in *Cirrus*, edited by D. K. Lynch et al., pp. 346–374, Oxford Univ. Press, New York.

Sassen, K., Z. Wang, V. I. Khvorostyanov, G. L. Stephens, and A. Bennedetti (2002), Cirrus cloud ice water content radar algorithm evaluation using an explicit cloud microphysical model, *J. Appl. Meteorol.*, *41*, 620–628.

Stephens, G. L., S. Tsay, P. W. Stackhouse, and P. J. Flatau (1990), The relevance of the microphysical and radiative properties of cirrus clouds to climate and climatic feedback, *J. Atmos. Sci.*, *47*, 1742–1754.

Wang, Z., and K. Sassen (2002), Cirrus cloud microphysical property retrieval using lidar and radar measurements. Part II: Midlatitude cirrus microphysical and radiative properties, *J. Atmos. Sci.*, *59*, 2291–2302.

Wylie, D. P., and W. P. Menzel (1999), Eight years of high cloud statistics using HIRS, *J. Clim.*, *12*, 170–184.

————————

R. Boers, D. P. Donovan, H. Klein Baltink, and G.-J. van Zadelhoff, Royal Netherlands Meteorological Institute, P. O. Box 201, NL-3730 AE De Bilt, Netherlands. (zadelhof@knmi.nl)